remote sensing

Article

A Sidelobe Suppression Method for Circular Ground-Based SAR 3D Imaging Based on Sparse Optimization of Radial Phase-Center Distribution

Qiming Zhang [1], Jinping Sun [1,*], Yanping Wang [2] and Yun Lin [2]

[1] School of Electronics & Information Engineering, Beihang University, Beijing 100191, China; by2102234@buaa.edu.cn
[2] School of Information Science & Technology, North China University of Technology, Beijing 100144, China; wangyp@ncut.edu.cn (Y.W.); ylin@ncut.edu.cn (Y.L.)
* Correspondence: sunjinping@buaa.edu.cn; Tel.: +86-10-8231-7240

Abstract: Circular ground-based SAR (GBSAR) is a new 3D imaging GBSAR with the potential of acquiring high-quality 3D SAR images and 3D deformation. However, its donut-shaped spectrum and short radius of antenna rotation cause high sidelobes on 3D curved surfaces, resulting in 3D SAR images with poor quality. The multi-phase-center circular GBSAR with full array can effectively suppress sidelobes by filling the donut-shaped spectrum to be the equivalent solid spectrum, but it requires a larger number of phase centers, increasing system cost and engineering difficulties. In this paper, a sidelobe suppression method for circular GBSAR 3D imaging based on sparse optimization of radial phase-center distribution is proposed to suppress high sidelobes at low cost. By deriving the point spread function (PSF) of multi-phase-center circular GBSAR and taking the peak sidelobe level (PSL) and integrated sidelobe level (ISL) of the derived PSF as multi-objective functions, we solve the multi-objective optimization problem to optimize the sparse distribution of radial phase centers. The advantage of the proposed method is that the solved optimal radial phase-center distribution can effectively suppress the 3D sidelobes of circular GBSAR with a limited number of phase centers. Finally, the sidelobe suppression effect of the proposed method is verified via 3D imaging simulations.

Keywords: circular ground-based SAR; 3D imaging; sidelobe suppression; sparse optimization; multi-objective optimization

check for updates

Citation: Zhang, Q.; Sun, J.; Wang, Y.; Lin, Y. A Sidelobe Suppression Method for Circular Ground-Based SAR 3D Imaging Based on Sparse Optimization of Radial Phase-Center Distribution. *Remote Sens.* **2022**, *14*, 3248. https://doi.org10.3390/rs14143248/

Academic Editors: Ali Khenchaf and Jean-Christophe Cexus

Received: 8 June 2022
Accepted: 4 July 2022
Published: 6 July 2022

1. Introduction

Ground-based Synthetic Aperture Radar (GBSAR) is a low-cost remote sensing instrument for deformation measurement [1]. Due to its outstanding advantages in deformation monitoring, such as all-day, high-precision, and continuous monitoring over a short period, GBSAR has been used in landslide monitoring, open-pit mine monitoring, ground subsidence monitoring, building monitoring, etc. [2,3]. Traditional linear GBSAR and ground-based ArcSAR can only acquire 2D images and are unable to acquire 3D images [4–6]. When they are used to monitor complex scenes such as terrain fluctuations, there will appear a "layover" phenomenon. The phenomenon restricts the application of measuring 3D deformation for terrain-fluctuation scenes [7,8]. Thus, research on GBSAR systems with fast acquisition of 3D high-quality images has become a hotspot in the field of deformation monitoring. In recent years, there has been a lot of research on GBSAR 3D imaging. At present, 3D imaging GBSAR includes multi- baseline linear GBSAR, multi-baseline ground-based ArcSAR, and circular GBSAR [9–11]. The multi-baseline linear GBSAR forms a 2D array aperture in the azimuth-vertical plane to acquire 3D SAR images [12–14]. The multi-baseline ground-based ArcSAR forms a curved array aperture on the azimuth-vertical curved surface to realize 3D imaging [15].

Circular GBSAR can obtain 3D imaging data by forming a 2D synthetic aperture with a single scan [16]. It has the advantages of convenient system structure, short data acquisition time, and strong timeliness of deformation monitoring. However, its donut-shaped spectrum and short radius of antenna rotation can cause high sidelobes on 3D curved surfaces [17]. In complex monitoring scenes, the high sidelobes of the strong target may cover the main lobes of nearby weak and small targets in the circular GBSAR image, resulting in poor image contrast and low image clarity. This problem seriously affects the 3D imaging quality of circular GBSAR.

The traditional methods, such as frequency domain windowing [18], spectrum reshaping [19], and spatially variant apodization filtering [20,21], are all based on using smooth spectrum edge to achieve sidelobe suppression of SAR images [22]. The sparse representation method is also one of the existing sidelobe suppression methods. It is a regularization optimization method based on sparse scene, and its point spread function (PSF) is impulse response [23]. However, none of them can effectively suppress the high sidelobe caused by the donut-shaped spectrum of circular GBSAR. At present, there are mainly two methods for sidelobe suppression of circular GBSAR: the circular array SAR with uniform and continuous spectrum distribution, and the circular GBSAR with sparse spectrum distribution. The method with uniform and continuous spectrum distribution broadens the radial width of the donut-shaped spectrum, achieving a slight suppression of the sidelobes in the array plane [24]. The method with sparse spectrum distribution optimizes the distribution of concentric donut-shaped spectrum and can achieve an obvious suppression of the sidelobes in the array plane [25]. However, the above two methods only consider the sidelobe suppression of circular GBSAR in the 2D plane, and the high sidelobes of circular GBSAR in the 3D curved surface are not considered.

The short radius of antenna rotation and the donut-shaped spectrum of circular GBSAR lead to 3D high sidelobes on two equidistant curved surfaces. One is orthogonal to the normal direction of the plane with antenna rotation, and the other is orthogonal to range. The multi-phase-center circular GBSAR method can be used to suppress the above high sidelobes, and the number and distribution of phase centers affect the spatial sampling density of the GBSAR. The sampling density of the spatial spectrum support domain is directly related to the sidelobe characteristics of imaging. The greater the density, the easier to control the sidelobe characteristics. Setting a large number of phase centers in the radial, the method of radial phase-center distribution with full array can fill the donut-shaped spectrum to obtain an equivalent solid spectrum, suppressing 3D high sidelobes. However, the system cost of the distribution with full array is high, and it is difficult to achieve in engineering.

In this paper, a sidelobe suppression method for circular GBSAR 3D imaging with sparse optimization of radial phase-center distribution is proposed. The proposed method considers the 3D sidelobe distribution of circular GBSAR on two equidistant curved surfaces. The PSFs of circular GBSAR on two equidistant curved surfaces are derived with the geometry of circular GBSAR and the imaging signal integral equation of the back-projection (BP) algorithm. Taking the peak sidelobe level (PSL) and integrated sidelobe level (ISL) of the PSF as the multi-objective function, we use the nondominated sorting genetic algorithm II (NSGA-II) to solve the multi-objective optimization problem, so as to optimize the sparse distribution of radial phase centers. Circular GBSAR based on the solved optimal sparse distribution is used to acquire the 3D images with the optimal sidelobe distribution under the condition of a given number of phase centers. Compared with the existing methods in references [24,25], the proposed method has a better sidelobe suppression effect and less time consumption by taking the PSL and ISL of the derived PSF as the multi-objective function and using NSGA-II to solve the optimization problem. The advantages of the proposed method are that the solved optimal radial phase-center distribution can effectively suppress the high sidelobes in circular GBSAR 3D imaging, further improving the 3D imaging quality of circular GBSAR. Moreover, the benefits of the proposed method are that it is helpful to obtain high-quality 3D images and accurate deformation of complex terrain areas.

The rest of this paper is organized as follows. Section 2 introduces the geometry and 3D sidelobe distribution of circular GBSAR. Section 3 presents the implementation of the sidelobe suppression method with sparse optimization of radial phase-center distribution. Section 4 shows some imaging results. Finally, Section 5 concludes the paper.

2. Geometry and 3D Sidelobe Distribution of Circular GBSAR

The geometry of circular GBSAR is shown in Figure 1. The antenna phase center (APC) a is fixed at the end point A of the rotating arm, and makes a circular motion around the rotating center O. The antenna beam center points to the normal direction of the plane with antenna rotation. A 2D circular synthetic aperture orthogonal to range can be formed by rotating the APC a. The point P_t in Figure 1 is taken as an example. Due to the relatively small radius of antenna rotation, the point spread function (PSF) of circular GBSAR is mainly distributed in range, the equidistant curved surface S1 orthogonal to range, and the equidistant curved surface S2 orthogonal to the AP_t direction. Because the PSF of circular GBSAR has the characteristic of circular symmetry, we can use the PSFs in the equidistant curves Curve1 and Curve2, as shown in Figure 1, to describe the PSFs on the equidistant curved surfaces S1 and S2, respectively. Thus, we derive the PSFs in range, Curve1 and Curve2, to analyze the 3D sidelobe distribution of circular GBSAR.

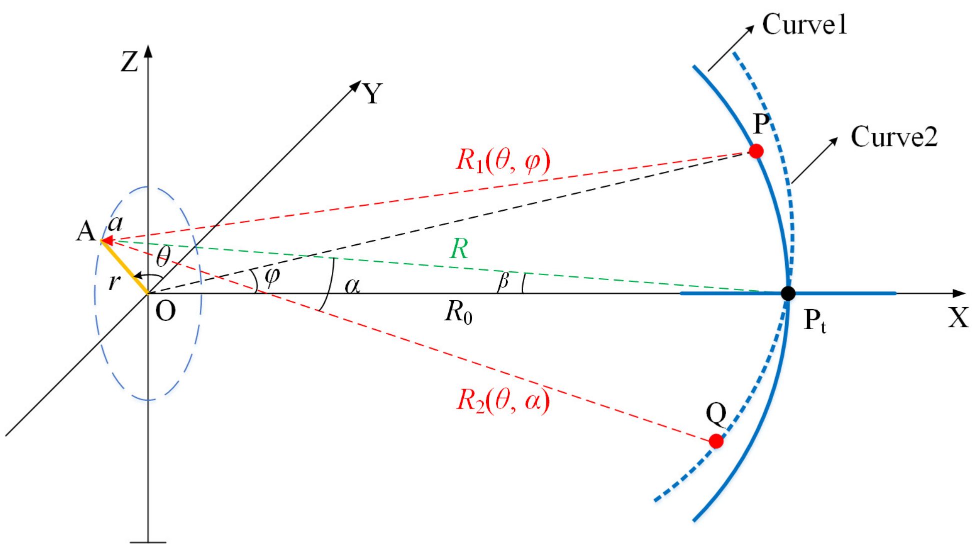

Figure 1. Geometry and 3D sidelobe distribution of circular GBSAR.

In Figure 1, r is the rotation radius of the APC a, θ is the instantaneous rotation angle of the APC a, β is the angle between OP_t and AP_t, and φ is the angle between OP_t and OP. Where, P_t is a point target at the scene center, P is a point in Curve1, and R_0 is the distance from the antenna rotation center O to the point target P_t. It can be seen from the geometry of circular GBSAR that the distance from the APC a to the point target P_t is:

$$R = \sqrt{R_0^2 + r^2}. \tag{1}$$

The distance from the APC a to any pixel point P in Curve1 is:

$$R_1(\theta, \varphi) = \sqrt{R_0^2 + r^2 - 2rR_0 \sin\varphi \cos\theta}. \tag{2}$$

The distance from the APC a to any pixel point Q in Curve2 is:

$$R_2(\theta, \alpha) = \sqrt{R^2 + 2r^2(1 - \cos\theta) + 2rR\sin(\alpha - \beta)(1 - \cos\theta)}, \tag{3}$$

where α is the angle between AP_t and AQ.

The PSF of circular GBSAR in range has been derived in literature [26], and it is similar to the Sinc function. Thus, we only need to derive the PSFs of circular GBSAR in Curve1 and Curve2, to describe its 3D sidelobe distribution. Since the spectrum of circular GBSAR in Curve1 and Curve2 is not easy to solve, we use the imaging signal integral equation of the back-projection (BP) algorithm to derive the PSFs of circular GBSAR in Curve1 and Curve2. Taking the linear frequency modulation (LFM) signal as the transmitted signal, the preprocessed echo signal can be expressed as:

$$f_{\mathrm{e}}(K) = \sigma \cdot \exp\{-jKR\}, \tag{4}$$

where σ is the backscattering coefficient, and $\sigma = 1$; K is the wave number of the transmitted signal, $K = 4\pi f/c$, and $K \in [K_{\min}, K_{\max}]$.

First, we derive the PSF of circular GBSAR in Curve1. The BP imaging signal of circular GBSAR in Curve1 can be expressed as:

$$g(\varphi) \approx \iint K \exp\{-jKR\} \cdot \exp\{jKR_1(\theta,\varphi)\} d\theta dK. \tag{5}$$

Substituting Equations (1) and (2) into the above integral equation, we can get the integral equation:

$$\begin{aligned} g(\varphi) &\approx \int_{K_{\min}}^{K_{\max}} K\left\{\int_0^{2\pi} \exp[jK(R_1(\theta,\varphi) - R)]d\theta\right\}dK \\ &= \int_{K_{\min}}^{K_{\max}} K\left\{\int_0^{2\pi} \exp\left[jK\left(\sqrt{R_0^2 + r^2 - 2rR_0 \sin\varphi\cos\theta} - \sqrt{R_0^2 + r^2}\right)\right]d\theta\right\}dK. \end{aligned} \tag{6}$$

Since the integral in Equation (6) contains the radical term, it is difficult to be directly solved. Thus, we approximate the radical term to facilitate solving the integral. The radical term in Equation (6) can be expressed as:

$$\begin{cases} m_1(r) = \sqrt{R_0^2 + r^2 - 2rR_0\sin\varphi\cos\theta} \\ n_1(r) = \sqrt{R_0^2 + r^2} \end{cases}. \tag{7}$$

The first-order Taylor series expansion of Equation (7) about r can be approximated as:

$$\begin{cases} m_1(r) = m_1(0) + m_1'(0) \cdot r + \mathrm{O}_1(r) \approx R_0 - r\sin\varphi\cos\theta \\ n_1(r) = n_1(0) + n_1'(0) \cdot r + \mathrm{O}_1(r) \approx R_0 \end{cases}. \tag{8}$$

Substituting the approximation in Equation (8) into the integral of Equation (6), it can be simplified to:

$$g(\varphi) \approx \int_{K_{\min}}^{K_{\max}} K\left[\int_0^{2\pi} \exp(-jKr\sin\varphi\cos\theta)d\theta\right]dK. \tag{9}$$

By solving the integral in Equation (9), we can derive the PSF of circular GBSAR in Curve1.

$$\begin{aligned} g(\varphi) \approx &\int_{K_{\min}}^{K_{\max}} K \cdot J_0(Kr\sin\varphi)dK \\ &\approx \frac{2}{K_{\max}^2 - K_{\min}^2} \cdot \frac{K_{\max}J_1(K_{\max}r\sin\varphi) - K_{\min}J_1(K_{\min}r\sin\varphi)}{r\sin\varphi}. \end{aligned} \tag{10}$$

Next, we derive the PSF of circular GBSAR in Curve2. The BP imaging signal of circular GBSAR in Curve2 can be expressed as:

$$h(\alpha) \approx \iint K \exp\{-jKR\} \cdot \exp\{jKR_2(\theta,\alpha)\} d\theta dK. \tag{11}$$

Equation (3) is substituted into Equation (11) to solve the integral equation.

$$
\begin{aligned}
h(\alpha) &\approx \int_{K_{\min}}^{K_{\max}} K\left\{\int_0^{2\pi} \exp[jK(R_2(\theta,\alpha)-R)]d\theta\right\}dK \\
&= \int_{K_{\min}}^{K_{\max}} K\left\{\int_0^{2\pi} \exp\left[jK\left(\sqrt{R^2+2r^2(1-\cos\theta)+2rR\sin(\alpha-\beta)(1-\cos\theta)}-R\right)\right]d\theta\right\}dK.
\end{aligned} \tag{12}
$$

To facilitate solving the integral equation, we approximate the radical term in Equation (12). The radical term can be expressed as:

$$
m_2(r) = \sqrt{R^2+2r^2(1-\cos\theta)+2rR\sin(\alpha-\beta)(1-\cos\theta)}, \tag{13}
$$

where $\beta = \arctan(r/R_0)$, the rotation radius r is much smaller than the target distance R_0, so the angle β can be approximated to zero. The first-order Taylor series expansion of Equation (13) about r can be approximated as:

$$
m_2(r) = m_2(0) + m_2'(0)\cdot r + \mathrm{O}_1(r) \approx R + r\sin\alpha(1-\cos\theta). \tag{14}
$$

Substituting the approximation in Equation (14) into Equation (12), it can be simplified to:

$$
h(\alpha) \approx \int_{K_{\min}}^{K_{\max}} K\left\{\int_0^{2\pi} \exp[jKr\sin\alpha(1-\cos\theta)]d\theta\right\}dK. \tag{15}
$$

By solving the integral about θ in Equation (15), the 1-D integral equation of circular GBSAR in Curve2 can be further derived as:

$$
h(\alpha) \approx \int_{K_{\min}}^{K_{\max}} K\cdot J_0(Kr\sin\alpha)\cdot \exp\{jKr\sin\alpha\}dK. \tag{16}
$$

The analytical expression of the integral in Equation (16) is difficult to solve, and the computational efficiency of simulating PSF using the integral in Equation (16) is extremely low. Thus, we use the numerical method to derive the numerical solution of the PSF of circular GBSAR in Curve2.

$$
h(\alpha) \approx \sum_{i=1}^{N_k} K_i\cdot J_0(K_i r\sin\alpha)\cdot \exp\{jK_i r\sin\alpha\}\cdot dK, \tag{17}
$$

where N_k is the sampling points of the wave number K. dK is the sampling interval, $dK = (K_{\max} - K_{\min})/N_k$. K_i is the wave number of the i-th sampling point.

According to the simulation parameters in Table 1, we use Equations (10) and (17) to simulate the PSFs as shown in Figure 2, to observe the sidelobe distribution of circular GBSAR in Curve1 and Curve2.

Table 1. Simulation parameters.

Parameter	Value
Center frequency (GHz)	17.55
Bandwidth (MHz)	900
Rotation radius (m)	1
Azimuth beam width (°)	30
Vertical beam width (°)	30

Figure 2a,b show the overall sidelobe trend of the PSFs in Curve1 and Curve2. Figure 2c,d show the sidelobe distribution near the main lobe of the above PSFs.

It can be seen from Figure 2a,b that the PSF of circular GBSAR in Curve1 is similar to the first-order Bessel function of the first kind, and the sidelobe away from the main lobe of the PSF in Curve2 shows a trend with slowly oscillating attenuation. It can be seen from Figure 2c,d that the PSFs of circular GBSAR in Curve1 and Curve2 have high sidelobes, and their maximum sidelobes are up to −8 dB. In summary, the 3D high sidelobes of circular GBSAR are mainly concentrated on the equidistant curved surfaces. Thus, the high sidelobe of circular GBSAR 3D imaging can be suppressed by suppressing the sidelobes of the PSFs in Curve1 and Curve2.

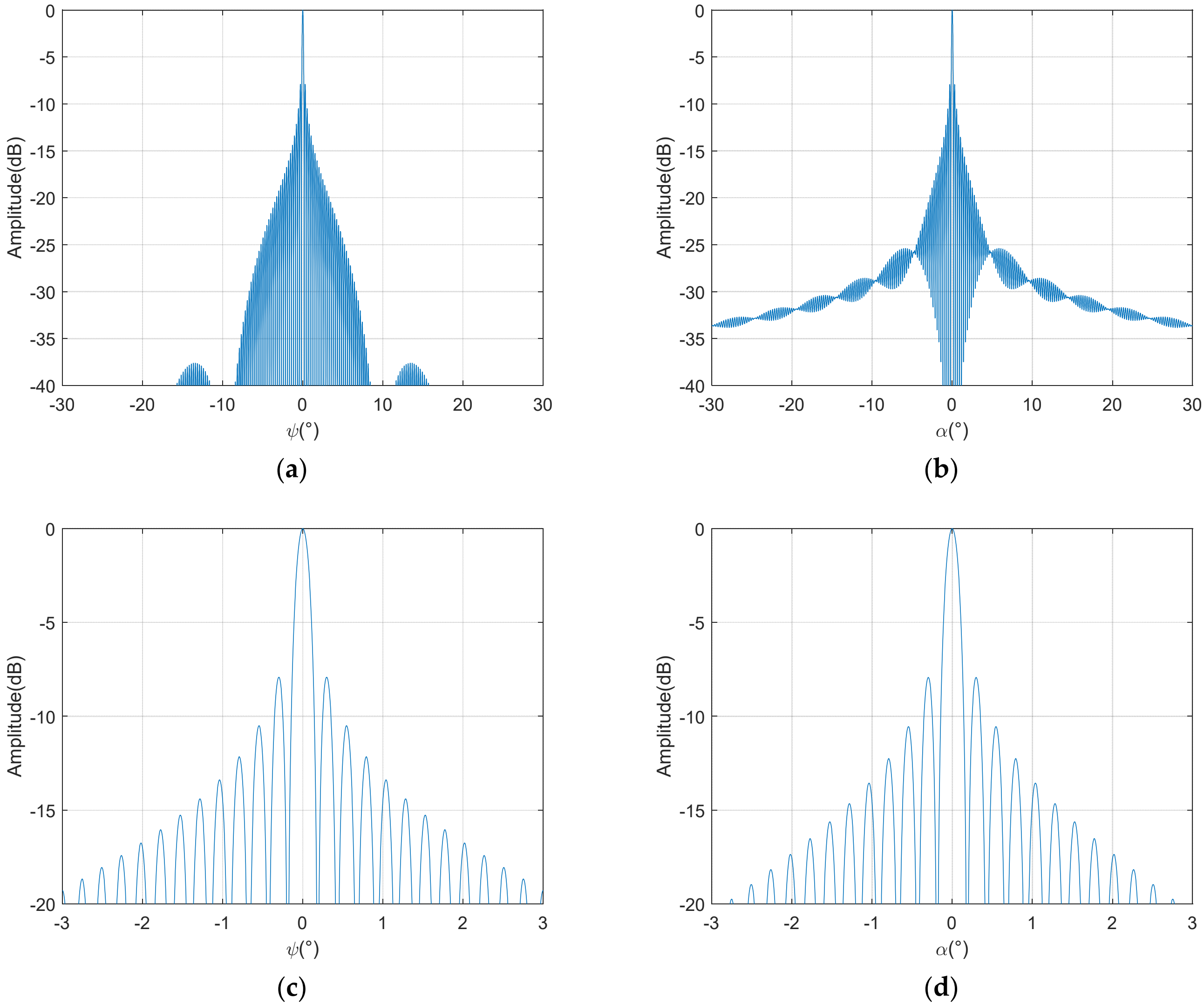

Figure 2. PSFs of circular GBSAR in Curve1 and Curve2: (**a**) PSF in Curve1 above −40 dB; (**b**) PSF in Curve2 above −40 dB; (**c**) PSF in Curve1 above −20 dB; (**d**) PSF in Curve2 above −20 dB.

3. Sidelobe Suppression Method for Circular GBSAR 3D Imaging

In the second section, the geometry of circular GBSAR has been introduced, and its 3D sidelobe distribution has also been analyzed. For the high sidelobes of circular GBSAR are mainly concentrated on the equidistant surface, based on the geometry of multi-phase-center circular GBSAR, we fill the hollow spectrum with frustum shaped of circular GBSAR to realize the 3D sidelobe suppression. Firstly, the point spread function (PSF) of multi-phase-center circular GBSAR on the equidistant curve is derived. Then, we solve the multi-objective optimization problem to obtain the optimal phase-center distribution with better 3D sidelobe suppression effect. Finally, we analyze the generality of the proposed method with different number of phase centers.

3.1. PSF of Multi-Phase-Center Circular GBSAR

To derive the PSF of multi-phase-center circular GBSAR, we present the geometry of multi-phase-center circular GBSAR in Figure 3. The antenna array $a_1, a_2, \ldots, a_N$ is fixed on the rotating arm at a certain interval, rotating around the rotation center O. Their antenna beam centers point in the normal direction of the plane with antenna rotation. Taking the point $\mathrm{P_t}$ in Figure 3 as an example, the synthetic aperture of the antenna array is a set of concentric rings, so its spectrum support domain is a set of hollow spectrums with frustum shaped. Therefore, the PSF of multi-phase-center circular GBSAR can be obtained by superposing the PSFs of multiple single-phase-center circular GBSAR.

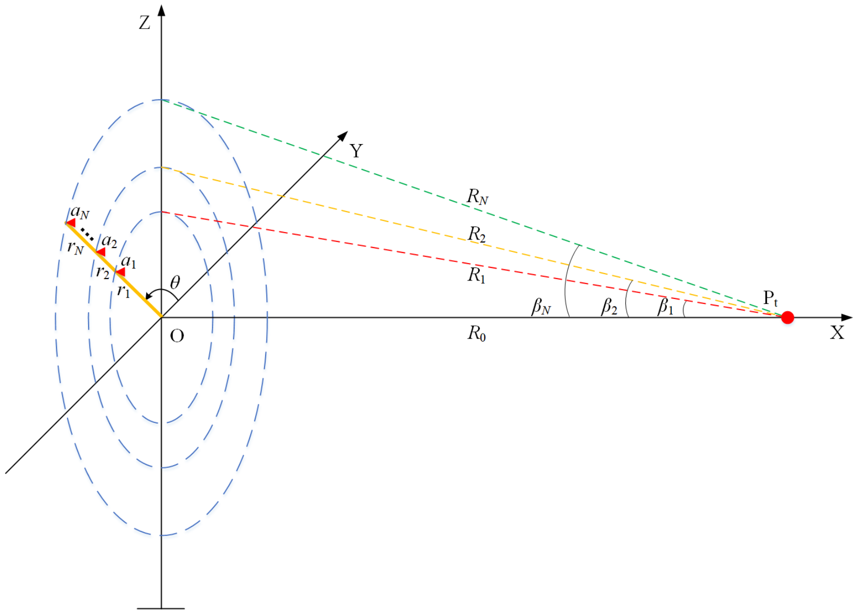

Figure 3. Geometry of multi-phase-center circular GBSAR.

In Figure 3, $r_1, r_2, \ldots, r_N$ are the rotation radius of the antenna array $a_1, a_2, \ldots, a_N$, θ is the instantaneous rotation angle of the antenna array $a_1, a_2, \ldots, a_N$, $\mathrm{P_t}$ is a point target at the scene center. $\beta_1, \beta_2, \ldots, \beta_N$ are the angles between $\mathrm{OP_t}$ and the direction from the antenna array to the point target $\mathrm{P_t}$, and $R_1, R_2, \ldots, R_N$ are the distance from the antenna array to the point target $\mathrm{P_t}$.

The 3D high sidelobes of circular GBSAR are mainly distributed on the equidistant curved surface, and the PSF on the equidistant curved surface is circularly symmetric. Thus, we only need to derive the PSF of multi-phase-center circular GBSAR in Curve1 and Curve2. The PSF of multi-phase-center circular GBSAR in Curve1 is:

$$g_m(\varphi) = \sum_{n=1}^{N} g(r_n, \varphi) \approx \frac{2}{K_{\max}^2 - K_{\min}^2} \cdot \sum_{n=1}^{N} \frac{K_{\max} J_1(K_{\max} r_n \sin\varphi) - K_{\min} J_1(K_{\min} r_n \sin\varphi)}{r_n \sin\varphi}, \tag{18}$$

where r_n is the rotation radius of the APC a_n.

The PSF of multi-phase-center circular GBSAR in Curve2 is:

$$h_m(\alpha) = \sum_{n=1}^{N} h(r_n, \alpha) \approx \sum_{n=1}^{N} \sum_{i=1}^{N_k} K_i \cdot J_0(K_i r_n \sin\alpha) \cdot \exp\{jK_i r_n \sin\alpha\} \cdot dK. \tag{19}$$

In summary, the PSFs in Curve1 and Curve2 of multi-phase-center circular GBSAR are both related to the phase-center distribution $r_1, r_2, \ldots, r_N$ of the antenna array $a_1, a_2, \ldots, a_N$. Thus, under the condition of a given number of phase centers, the sidelobe distribution of multi-phase-center circular GBSAR in Curve1 and Curve2 can be changed by optimizing radial phase-center distribution.

3.2. Sparse Optimization Method of Radial Phase-Center Distribution

According to Sections 2 and 3.1, the 3D high sidelobes of multi-phase-center circular GBSAR in Curve1 and Curve2 vary with the radial phase-center distribution. In this section, a sparse optimization method of radial phase-center distribution is introduced to optimize the sidelobe distribution of multi-phase-center circular GBSAR. Peak sidelobe level (PSL) and integrated sidelobe level (ISL) are two parameters used to describe the sidelobe distribution. If only the PSL is used as the objective function of optimization, it will lead to the higher ISL and the grating lobes. Thus, we construct a multi-objective optimization problem by taking the maximum PSL and ISL of the PSFs in Curve1 and Curve2 as the two objective functions and taking phase-center distribution as the decision variable. The nondominated sorting genetic algorithm II (NSGA-II) is used to solve the above multi-objective optimization problem, so as to optimize the phase-center distribution of circular GBSAR. Under the condition of a given number of phase centers, the method can obtain the optimal phase-center distribution with better sidelobe distribution, to realize the sidelobe suppression of circular GBSAR 3D imaging.

First, taking the maximum PSL and ISL of multi-phase-center circular GBSAR in Curve1 and Curve2 as the optimized objective functions, we construct the mathematical model of the minimization multi-objective optimization problem with 2 objective functions and $N-1$ decision variables.

$$\begin{aligned} &\min \boldsymbol{y} = F(\boldsymbol{r}) = (F_1(\boldsymbol{r}), F_2(\boldsymbol{r}))^{\mathrm{T}} \\ &\text{s.t. } 0 < \boldsymbol{r} < 1 \end{aligned} \tag{20}$$

where $\boldsymbol{r}$ is the decision variable, and $\boldsymbol{r} = (r_1, r_2, \ldots, r_{N-1}) \in X$. $\boldsymbol{y}$ is the optimized multi-objective function, and $\boldsymbol{y} = (y_1, y_2) \in Y$. X is the decision space, and Y is the objective space. $F_1(\boldsymbol{r})$ is the maximum PSL of the PSFs in Curve1 and Curve2, and $F_2(\boldsymbol{r})$ is the maximum ISL of the PSFs in Curve1 and Curve2.

$$\begin{cases} F_1(\boldsymbol{r}) = \max\{PSL_{c1}(\mathbf{r}), PSL_{c2}(\mathbf{r})\} \\ F_2(\boldsymbol{r}) = \max\{ISL_{c1}(\mathbf{r}), ISL_{c2}(\mathbf{r})\} \end{cases}, \tag{21}$$

where $PSL_{c1}(\boldsymbol{r})$ is the PSL of the PSF in Curve1, and $PSL_{c2}(\boldsymbol{r})$ is the PSL of the PSF in Curve2. $ISL_{c1}(\boldsymbol{r})$ is the ISL of the PSF in Curve1, and $ISL_{c2}(\boldsymbol{r})$ is the ISL of the PSF in Curve2.

$$\begin{cases} PSL_{c1}(\boldsymbol{r}) = 20\log_{10}\{\max|[g_m(\varphi) - g_{main}(\varphi)]/\mathrm{P}_g|\} \\ PSL_{c2}(\boldsymbol{r}) = 20\log_{10}\{\max|[h_m(\alpha) - h_{main}(\alpha)]/\mathrm{P}_h|\} \end{cases} \tag{22}$$

$$\begin{cases} ISL_{c1}(\boldsymbol{r}) = 10\log_{10}\left\{\left[\sum g_m^2(\varphi) - \sum g_{main}^2(\varphi)\right]/\sum g_{main}^2(\varphi)\right\} \\ ISL_{c2}(\boldsymbol{r}) = 10\log_{10}\left\{\left[\sum h_m^2(\alpha) - \sum h_{main}^2(\alpha)\right]/\sum h_{main}^2(\alpha)\right\} \end{cases}, \tag{23}$$

where $g_{main}(\varphi)$ and $h_{main}(\alpha)$ are the main lobes of $g_m(\varphi)$ and $h_m(\alpha)$, respectively. P_g and P_h are the main lobe peak values of $g_m(\varphi)$ and $h_m(\alpha)$, respectively.

$$\begin{cases} g_{main}(\varphi) = g_m(\varphi) \cdot \mathrm{rect}(\varphi/\varphi_0) \\ h_{main}(\alpha) = h_m(\alpha) \cdot \mathrm{rect}(\alpha/\alpha_0) \end{cases}, \tag{24}$$

where φ_0 and α_0 are the first zero crossing of $g_m(\varphi)$ and $h_m(\alpha)$, respectively.

Then, the sparse optimization method of radial phase-center distribution based on NSGA-II is used to optimize the maximum PSL and ISL of multi-phase-center circular GBSAR. That is to solve the minimization multi-objective optimization problem in Equation (20). The NSGA-II includes initial population generation, Pareto sorting, and population evolution [27]. The proposed sparse optimization method of radial phase-center distribution based on NSGA-II is shown in Figure 4.

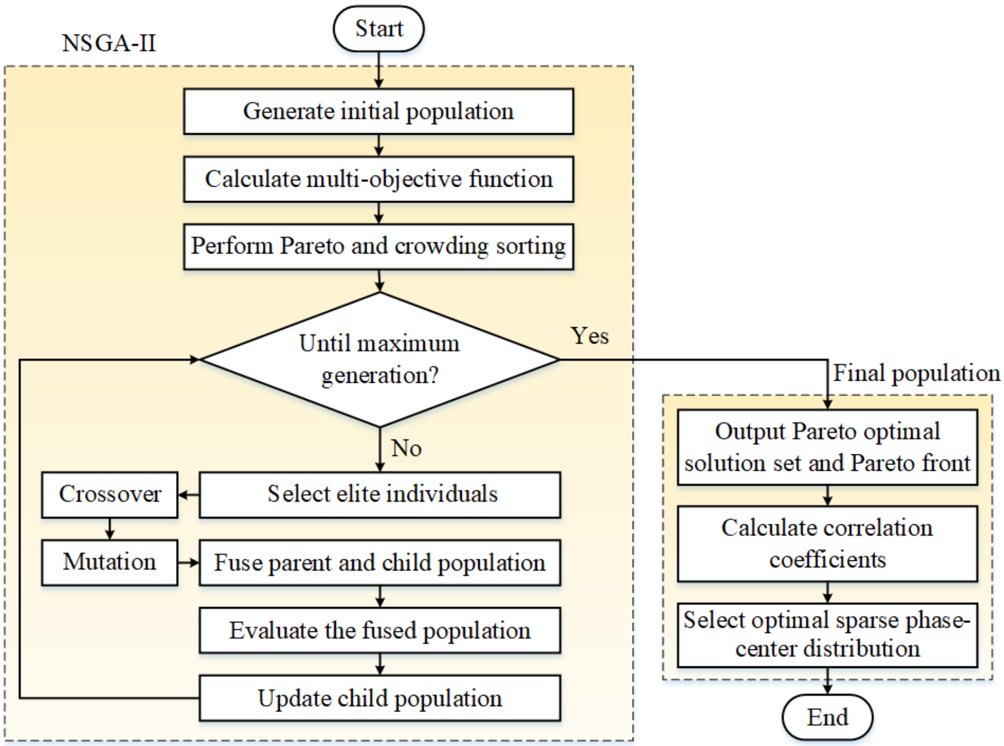

Figure 4. Framework of sparse optimization method of radial phase-center distribution.

According to the sidelobe suppression principle of multi-phase-center donut-shaped spectrum filling, the larger number of phase centers, the greater spectrum filling density, and the better sidelobe suppression effect. However, the larger number of phase centers will increase the system complexity and data size and reduce the system work efficiency. To obtain the optimal phase-center distribution with relatively good sidelobe suppression effect at low cost and high efficiency, under the condition of the number of phase centers $N = 3$, we construct the minimization multi-objective optimization problem with two objective functions and two decision variables. Then, we use the sparse optimization method of radial phase-center distribution based on NSGA-II to solve the optimal phase-center distribution. The optimization execution steps are summarized as follows.

Step 1: Generate the genes and chromosomes of initial populations.

After setting optimization parameters such as the individual number of the initial population, the initial population genes are generated by random numbers. The initial population chromosomes are generated by converting a set of binary numbers representing population genes into decimal numbers representing population chromosomes.

Step 2: Calculate the multi-objective function value of each individual in the current population, and perform Pareto sorting and crowding sorting.

According to the objective function in Equation (21), the multi-objective function values of population individuals can be calculated. Then, according to the Pareto dominance criterion, the population individuals corresponding to the above multi-objective function values are Pareto sorted, to obtain the Pareto optimal solution set of the initial population.

After obtaining the Pareto sorting result of the current population, the crowding distance between individuals with the same Pareto rank is calculated, and then the crowding degree is sorted with the crowding distance to maintain the diversity of individuals during the population evolution.

Step 3: Select, cross and mutate the genes of the parent population to generate the child population.

The selection operation randomly selects half the number of individuals from the parent population, and obtains the gene, Pareto rank and crowding degree information of the selected individuals. Then, the individual with the highest Pareto rank and the largest crowding distance is selected in turn, to replace an individual in the parent population.

The crossover operation randomly selects two gene positions of an individual and sorts them in ascending order. Then, the above genes are exchanged with the genes at the same positions of the latter individual.

The mutation operation randomly generates an array of the same dimension as the population genes and extracts the index positions of the zero element in the array. Next, we invert the binary values of the selected and crossed child population at the above index positions to achieve mutation.

Step 4: Fuse the parent and child populations, and evaluate the fused population.

Firstly, we fuse the genes of parent population and child population, and generate the chromosomes of the fused population through binary to decimal conversion. Then, the multi-objective function value of chromosomes in the fusion population is calculated. Finally, we perform Pareto sorting and crowding sorting on the fused population.

Step 5: Update the genes and chromosomes of the child population.

To retain the best individuals in the population and avoid the loss of excellent individuals in the selection process, we adopt the elite selection strategy of combining the parent and child populations. When the individual index of a Pareto rank reaches the population individual number, the crowding sorting of this Pareto rank is performed in descending order, and the individuals with larger crowding distance are selected to enter the new child population.

Step 6: Determine whether the maximum generation is reached.

If the maximum generation is not reached, the updated child population of the previous generation will be used as the parent population of the next generation, and steps 1 to 4 will be performed on it. If the maximum generation has been reached, the Pareto optimal solution set of the current population will be output, it is also known as the Pareto front. Then, the solution in the Pareto optimal solution set, whose PSF closest to the weighted Sinc function is selected as the optimal solution of the multi-objective optimization problem. Finally, the output optimal solution is the optimal phase-center distribution of multi-phase-center circular GBSAR.

For the multi-objective optimization problem of Equation (20), the population individual number is set to 200, and the individual chromosome number is set to 2. When the minimum interval of the phase-center distribution is 0.01 and the value range of the phase-center distribution is (0, 1), a 7-bit binary number is required to represent the genes of each chromosome. If the decimal number converted from the 7-bit binary number is greater than 1, it will be set to 1 to limit the value range of the chromosome. In addition, the selection proportion, crossover probability and mutation probability of population individuals in each generation are set to 0.5, 0.95 and 0.05, respectively. Moreover, the maximum generation is set to 100, and the algorithm will keep iterating until the maximum generation is reached. The distribution of the Pareto optimal solution set obtained with the above parameters is as shown in Figure 5a. Where, the blue circle represents the Pareto optimal solution set. The horizontal axis is the phase center r_1, and the vertical axis is the phase center r_2.

Figure 5a shows that the distribution range of r_1 in the Pareto optimal solution set is [0.44, 0.48], and the distribution range of r_2 is [0.65, 0.74]. To select the optimal solution of the multi-objective optimization problem from the Pareto optimal solution set, the Pareto front distributions of two objective functions are as shown in Figure 5b. Where, the green points connected by dotted lines constitute the Pareto front of the initial population, and the black points connected by solid lines are the Pareto front of the final population. The horizontal axis is the objective function $F_1(\boldsymbol{r})$, and the vertical axis is the objective function $F_2(\boldsymbol{r})$.

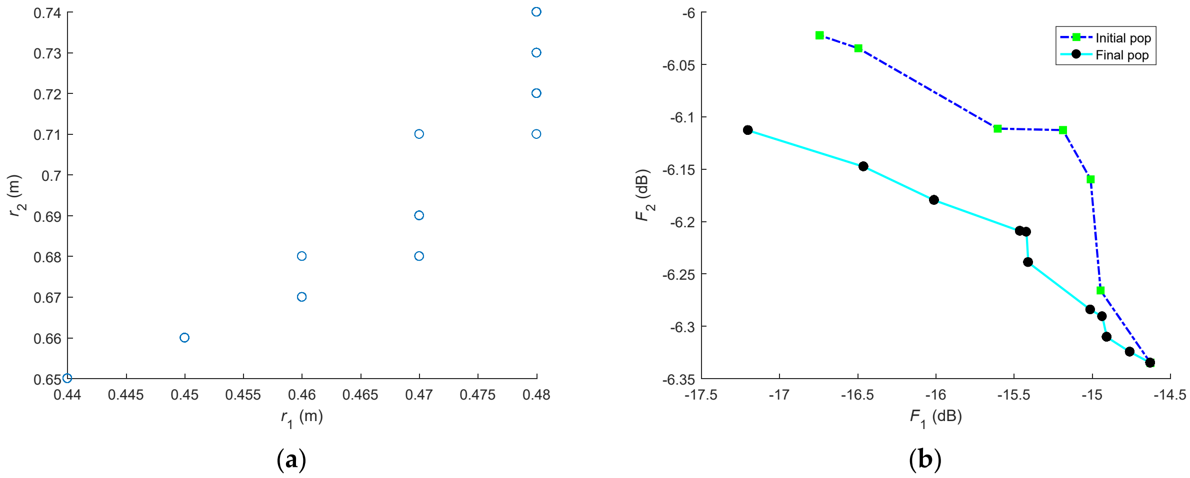

Figure 5. Distributions of Pareto optimal solution set and Pareto front with N = 3: (**a**) Pareto optimal solution set; (**b**) Pareto front.

Figure 5b shows that the Pareto front of the final population is better than that of the initial population. It indicates that the sparse optimization method of radial phase-center distribution is effective. To find the optimal phase-center distribution with better sidelobe suppression effect from Pareto optimal solution set, we analyze the similarity between the PSFs of all solutions in Pareto front and the weighted Sinc function by solving their correlation coefficients. Where, the weighted Sinc function is obtained by weighting the standard Sinc function with a −15 dB Taylor window function. Figure 6 shows the relationship between the Pareto optimal solution set and the obtained correlation coefficients. The larger correlation coefficient, the higher similarity with the weighted Sinc function. The Pareto optimal solution corresponding to the PSF with the highest similarity to the weighted Sinc function is the optimal phase-center distribution.

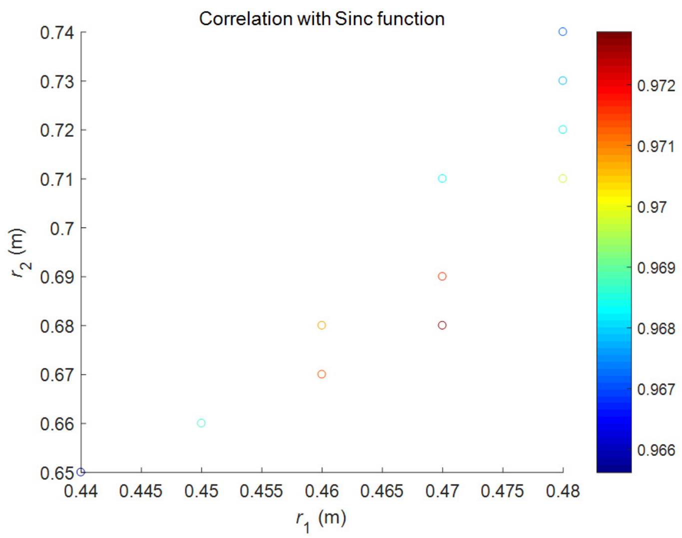

Figure 6. Correlation coefficients of Pareto optimal solutions with N = 3.

It can be seen from Figure 6 that the optimal phase-center distribution obtained by the proposed method is $r_1 = 0.47$, $r_2 = 0.68$, and $r_3 = 1$ under the condition of $N = 3$. The optimal PSL of circular GBSAR with the optimal phase-center distribution is −15.30 dB, and its optimal ISL is −6.16 dB. The above analysis shows that the proposed method can effectively suppress the high sidelobes of circular GBSAR.

3.3. Generality Analysis

In this section, to verify the applicability of the proposed method for sidelobe suppression of circular GBSAR with different number of phase centers, we mainly analyze the sidelobe suppression effect of the proposed method under the condition of the number of phase centers $N = 4$. The problem of optimizing the phase-center distribution with $N = 4$ can be transformed into a minimization multi-objective optimization problem with 2 objective functions and 3 decision variables. In addition to changing the individual chromosome number to 3, other parameters remain unchanged. Figure 7a shows the Pareto optimal solution set distribution after 100 generations. As we can see from Figure 7a that the range of r_1 in the Pareto optimal solution set is [0.33, 0.42], the range of r_2 is [0.54, 0.63], and the distribution range of r_3 is [0.69, 0.83]. Figure 7b shows that the Pareto front has about two objective functions $F_1(\boldsymbol{r})$ and $F_2(\boldsymbol{r})$.

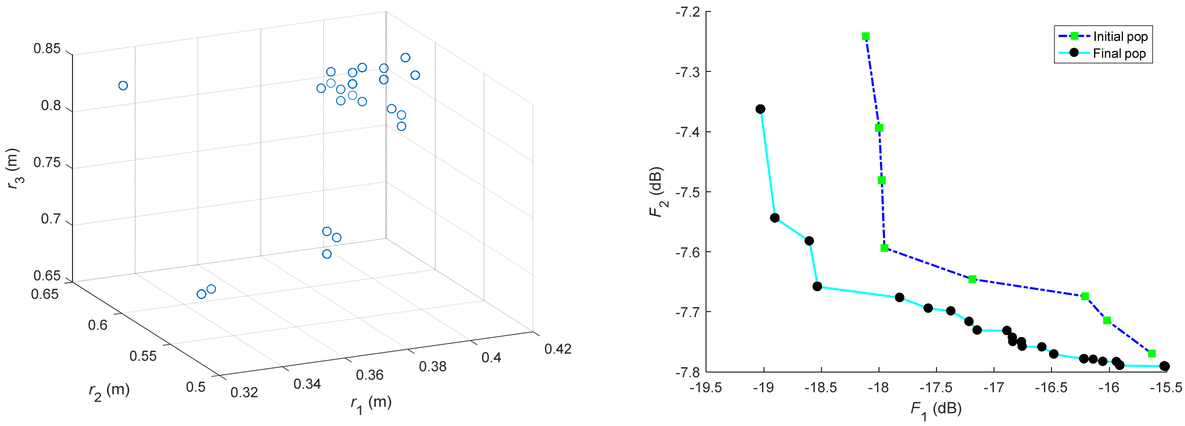

(**a**) (**b**)

Figure 7. Distributions of Pareto optimal solution set and Pareto front with $N = 4$: (**a**) Pareto optimal solution set; (**b**) Pareto front.

It can be seen from Figure 7b that the Pareto optimal solution set of the final population is also better than that of the initial population, under the condition of $N = 4$. It indicates that the proposed method is also suitable for optimizing the phase-center distribution with different number of phase centers. By calculating the correlation coefficient between the PSFs of the Pareto optimal solution set with $N = 4$ and the weighted Sinc function, we can obtain the relationship between the Pareto optimal solution set and the calculated correlation coefficients as shown in Figure 8.

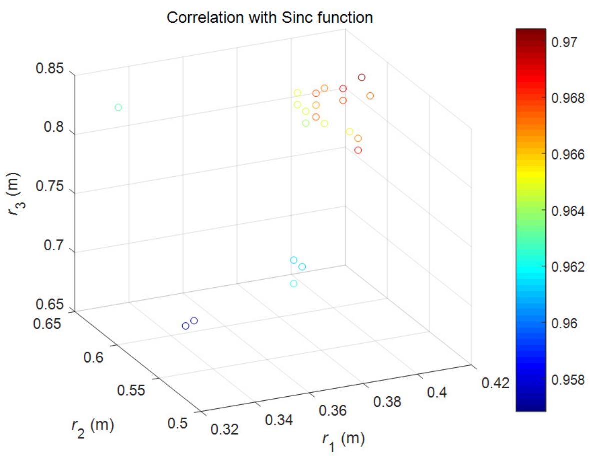

Figure 8. Correlation coefficients of Pareto optimal solutions with $N = 4$.

Figure 8 shows that the optimal phase-center distribution obtained by the proposed method is $r_1 = 0.42$, $r_2 = 0.63$, $r_3 = 0.82$, and $r_4 = 1$, under the condition of the number of phase centers $N = 4$. The optimal PSL of circular GBSAR with the optimal phase-center distribution is -15.08 dB, and its optimal ISL is -7.71 dB. The results show that, for multi-phase-center circular GBSAR with the different number of phase centers, the proposed method can also suppress its high sidelobes in 3D imaging.

To analyze the generality of the proposed method under the conditions of different number of phase centers, we compare the sidelobe suppression effects of multi-phase-center circular GBSAR with $N = 2, 3, 4, 5$, taking the sidelobe of circular GBSAR with $N = 1$ as the original sidelobe. Table 2 shows the optimal PSL and ISL solved by the proposed method under the conditions of the different number of phase centers. In addition to number of phase centers, other parameters are unchanged.

Table 2. Comparison of the sidelobe suppression effects.

Number of Phase Centers	Distribution (m)	PSL (dB)	ISL (dB)
$N = 1$	{1}	−7.91	−0.86
$N = 2$	{0.59, 1}	−13.07	−4.02
$N = 3$	{0.47, 0.68, 1}	−15.30	−6.16
$N = 4$	{0.42, 0.63, 0.82, 1}	−15.08	−7.71
$N = 5$	{0.31, 0.50, 0.63, 0.78, 1}	−19.75	−8.91

It can be seen from Table 2 that the larger number of phase centers, the better sidelobe suppression effect. The optimal PSL and ISL of multi-phase-center circular GBSAR can be suppressed close to the sidelobe level of the weighted Sinc function, when the number of phase centers is set more than 3. However, a large number of phase centers will increase the system complexity and data size. Therefore, a compromise value should be chosen to satisfy good sidelobe suppression effect at low system cost. In summary, the proposed method can be applied to circular GBSAR with different number of phase centers, and the number can be adjusted in different applications.

4. Simulations

To verify the imaging quality and sidelobe suppression effect of the proposed method in circular GBSAR 3D imaging, we use the 3D back-projection (BP) algorithm to simulate the 3D imaging results of multiple point targets, with the simulation parameters shown in Tables 1 and 3.

Table 3. Distribution parameters of phase centers and point targets.

Parameters	Value
Range (m)	400~600
Azimuth (m)	−60~60
Vertical (m)	−60~60
Single phase center (m)	$r = 1$
Sparse multiple phase centers in [25] (m)	$r = \{0.42, 0.56, 1\}$
Optimal sparse multiple phase centers (m)	$r = \{0.47, 0.68, 1\}$
Multiple phase centers with equivalent solid spectrum (m)	$r = [0.37, 1]$, $N_s = 40$

In this section, taking the number of phase centers $N = 3$ as an example, we analyze the sidelobe suppression effect of the proposed method in circular GBSAR 3D imaging by comparing the imaging performance of point targets at different positions using circular GBSAR with four different distributions. These distributions include single-phase-center distribution, sparse multi-phase-center distribution in [25], optimal sparse multi-phase-center distribution, and multi-phase-center distribution with equivalent solid spectrum. Figure 9 shows the distribution of multiple point targets in 3D space. Figure 10 shows the 3D BP imaging results of multiple point targets by circular GBSAR with the above phase-center distributions.

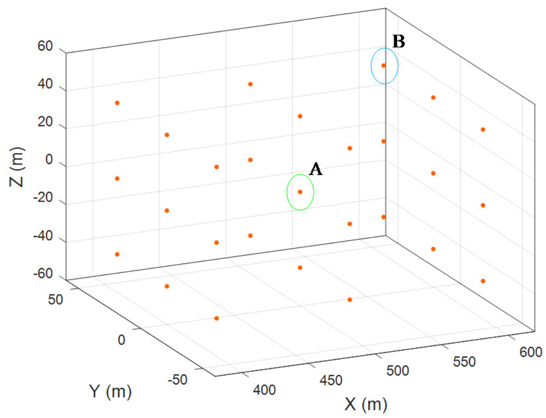

Figure 9. Spatial position distributions of multiple point targets.

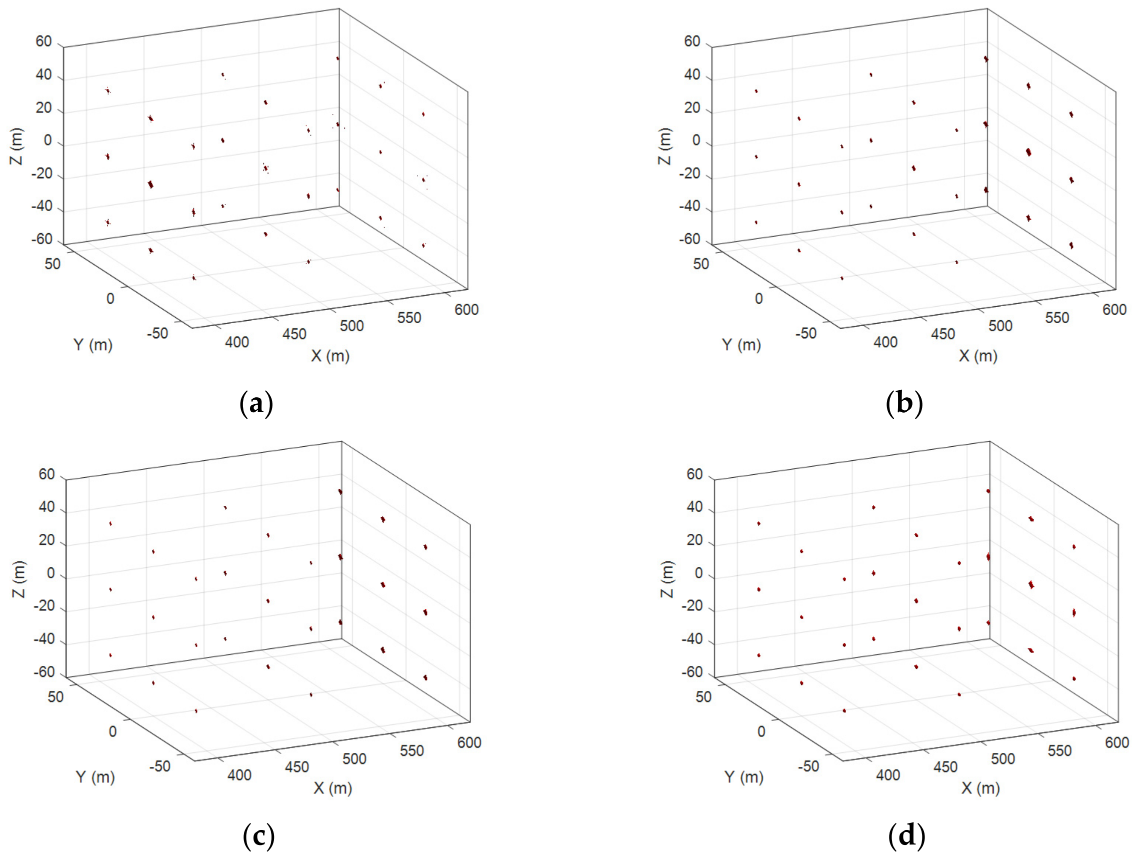

Figure 10. Three-dimensional BP imaging results of multiple point targets by using circular GBSAR with four different distributions: (**a**) Single-phase-center distribution; (**b**) Sparse multi-phase-center distribution in [25]; (**c**) Optimal sparse multi-phase-center distribution; (**d**) Multi-phase-center distribution with equivalent solid spectrum.

It can be seen from the 3D BP imaging results of circular GBSAR with four different distributions that the multiple point targets can be accurately focused on the target positions as shown in Figure 9. In Figure 10, the 3D BP imaging results of circular GBSAR with four different distributions have the nearly same range resolution, and their azimuth resolutions have the same trend. The farther range, the worse azimuth resolution. Figure 10a shows that the 3D imaging results of circular GBSAR based on single-phase-center distribution is affected by high sidelobes. Figure 10b–d show that the 3D imaging results of circular GBSAR based on the three multi-phase-center distribution are all better than that of single-phase-center distribution. It indicates that they can all improve the 3D imaging quality of circular GBSAR. However, there are some differences in the 3D image quality of circular GBSAR based on the above distribution.

To further compare the 3D imaging quality of circular GBSAR based on the above distributions, we quantitatively analyze the imaging quality of point targets at different positions. Point A (500, 0, 0) and point B (600, 40, 40) are selected to represent the point target at the scene center and the point target at the scene edge, respectively. In Figure 9, Point A is marked with a green circle, and Point B is marked with a blue circle. Figure 11 shows the 3D BP imaging results of point A by circular GBSAR based on single-phase-center distribution, sparse multi-phase-center distribution in [25], optimal sparse multi-phase-center distribution, and multi-phase-center distribution with an equivalent solid spectrum.

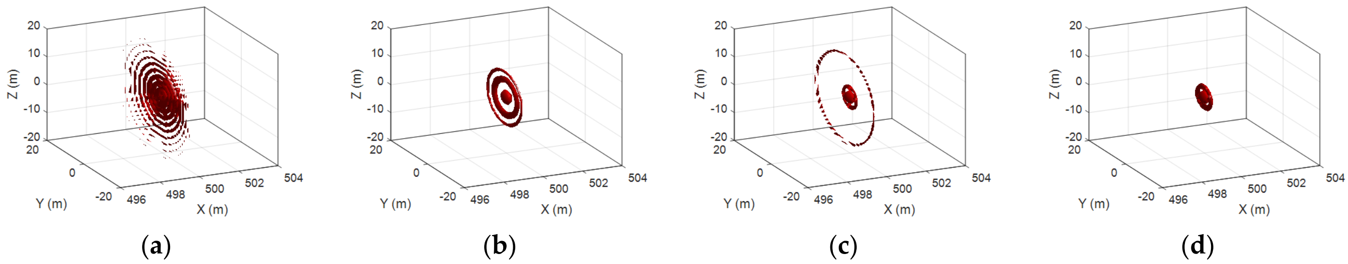

Figure 11. Three-dimensional BP imaging results of point A by circular GBSAR with different distributions: (**a**) Single-phase-center distribution; (**b**) Sparse multi-phase-center distribution in [25]; (**c**) Optimal sparse multi-phase-center distribution; (**d**) Multi-phase-center distribution with equivalent solid spectrum.

As we can see from Figure 11 that the optimal sparse multi-phase-center distribution solved by the proposed method has better 3D imaging quality than the sparse multi-phase-center distribution in [25] and single-phase-center distribution. Since the PSF results of circular GBSAR are mainly distributed in range and the equidistant curved surface, and the PSF results on the equidistant curved surface are distributed symmetrically, we can analyze the 3D imaging quality with the PSF results in range and the equidistant curve. To further analyze the sidelobe suppression effect of the proposed method on the point target at the scene center, Figures 12–14 show the PSF results of circular GBSAR in range, Curve1, and Curve2, respectively.

As shown in Figure 12, the PSF results in range by circular GBSAR with the four different distributions are almost identical, and they are all similar to the Sinc function. Figures 13a and 14a show that the sidelobes in Curve1 and Curve2 by circular GBSAR with single-phase-center distribution are high. It can be seen from Figures 13b,c and 14b,c that the sidelobes in Curve1 and Curve2 by circular GBSAR with optimal sparse multi-phase-center distribution are lower than that of the sparse multi-phase-center distribution in [25]. In addition, there are grating lobes in the PSF results of the sparse multi-phase-center distribution in [25], while the PSF results of the optimal sparse multi-phase-center distribution have better sidelobe distribution. As shown in Figures 13d and 14d, the sidelobes in Curve1 and Curve2 by circular GBSAR based on multi-phase-center distribution with equivalent solid spectrum are generally lower, while its decay rate is faster. Its PSF results in Curve1 and Curve2 are close to the form of the Sinc function, so it can be used as a reference for imaging quality analysis.

Table 4 shows the 3D imaging quality parameters of point A by circular GBSAR, including peak sidelobe ratio (PSLR), integrated sidelobe ratio (ISLR) and 3 dB impulse response width (IRW). It can be seen from Table 4 that the 3D imaging quality and the sidelobe suppression effect of circular GBSAR based on optimal sparse multi-phase-center distribution obtained by the proposed method.

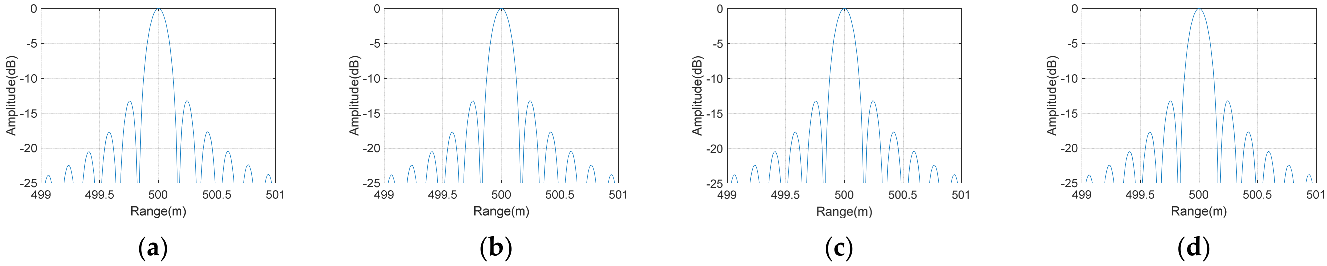

Figure 12. PSF results of point A in range: (**a**) Single-phase-center distribution; (**b**) Sparse multi-phase-center distribution in [25]; (**c**) Optimal sparse multi-phase-center distribution; (**d**) Multi-phase-center distribution with equivalent solid spectrum.

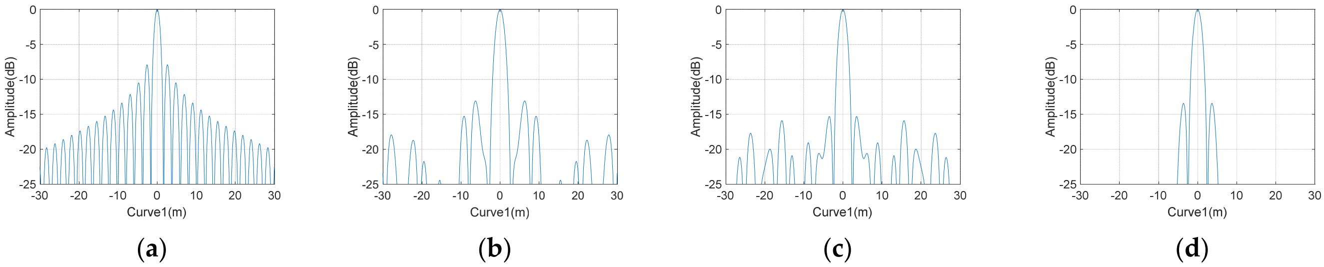

Figure 13. PSF results of point A in Curve1: (**a**) Single-phase-center distribution; (**b**) Sparse multi-phase-center distribution in [25]; (**c**) Optimal sparse multi-phase-center distribution; (**d**) Multi-phase-center distribution with equivalent solid spectrum.

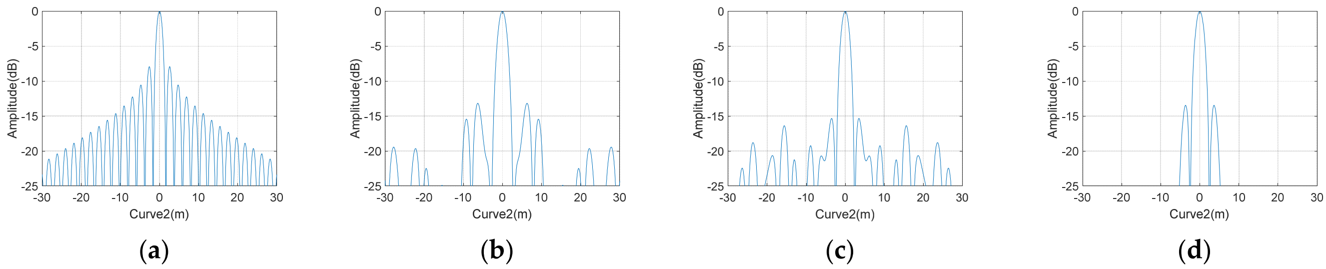

Figure 14. PSF results of point A in Curve2: (**a**) Single-phase-center distribution; (**b**) Sparse multi-phase-center distribution in [25]; (**c**) Optimal sparse multi-phase-center distribution; (**d**) Multi-phase-center distribution with equivalent solid spectrum.

Table 4. The 3D imaging quality analysis of point A.

Array Distribution	**Parameters**	**Range**	**Curve1**	**Curve2**
Single-phase-center distribution	IRW (m)	0.16	1.53	1.53
	PSLR (dB)	−13.22	−7.91	−7.92
	ISLR (dB)	−9.26	−1.19	−1.38
Sparse multi-phase-center distribution in [25]	IRW (m)	0.15	2.22	2.22
	PSLR (dB)	−13.23	−13.08	−13.16
	ISLR (dB)	−9.26	−5.59	−6.22
Optimal sparse multi-phase-center distribution	IRW (m)	0.16	2.07	2.07
	PSLR (dB)	−13.22	−15.31	−15.32
	ISLR (dB)	−9.26	−6.12	−6.42
Multi-phase-center distribution with equivalent solid spectrum	IRW (m)	0.15	2.17	2.17
	PSLR (dB)	−13.23	−13.43	−13.45
	ISLR (dB)	−9.26	−11.69	−11.75

As shown in Table 4, the PSLR and ISLR in Curve1 and Curve2 by circular GBSAR with optimal sparse multi-phase-center distribution are both lower than that of the circular GBSAR with the single-phase-center distribution. This shows that the proposed method can effectively suppress the high sidelobes on the 3D curved surface by circular GBSAR. We can see from Table 4 that in Curve1 and Curve2, the PSLR, ISLR and IRW of optimal sparse multi-phase-center distribution are all better than that of the sparse multi-phase-center distribution in [25]. This shows that the proposed method has better 3D sidelobe suppression effect than the method in [25]. Meanwhile, compared with the PSLR and ISLR of multi-phase-center distribution with equivalent solid spectrum, the proposed method can suppress the PSLR value on the 3D curved surface to be lower than the PSLR reference value under the condition of a limited number of phase centers. However, although the proposed method can obviously suppress the ISLR value on the 3D curved surface, it is still slightly higher than the ISLR reference value. This is a disadvantage of circular GBSAR with a fewer number of phase centers.

To verify the applicability of the proposed method for point targets in the whole observation scene, we select the point target B at the scene edge, analyzing its image quality. Figure 15 shows the 3D BP imaging results of point B by circular GBSAR based on single-phase-center distribution, sparse multi-phase-center distribution in [25], optimal sparse multi-phase-center distribution, and multi-phase-center distribution with an equivalent solid spectrum.

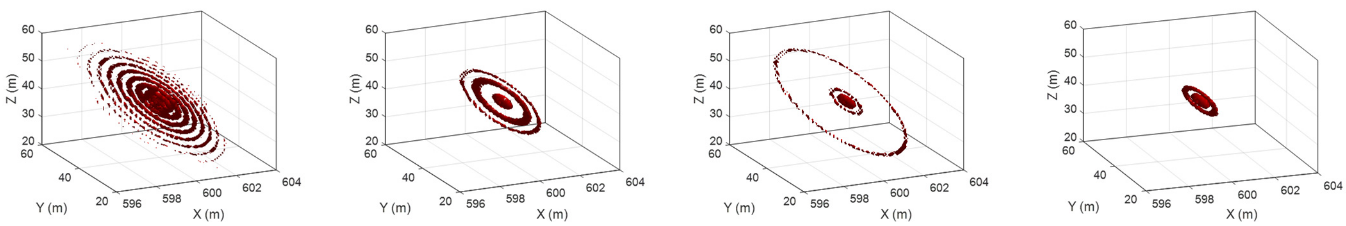

(**a**) (**b**) (**c**) (**d**)

Figure 15. Three-dimensional BP imaging results of point B by circular GBSAR with different distributions: (**a**) Single-phase-center distribution; (**b**) Sparse multi-phase-center distribution in [25]; (**c**) Optimal sparse multi-phase-center distribution; (**d**) Multi-phase-center distribution with equivalent solid spectrum.

It can be seen from Figure 15 that, compared with the method in [25], the proposed method is more effective to suppress the 3D high sidelobes of circular GBSAR for point targets at the scene edge. To further analyze the sidelobe suppression effect of the proposed method on the point target at the scene edge, we analyze its 3D imaging quality through the PSF results in range and the equidistant curve. Figures 16–18 show the PSF results of circular GBSAR in range, Curve1, and Curve2, respectively.

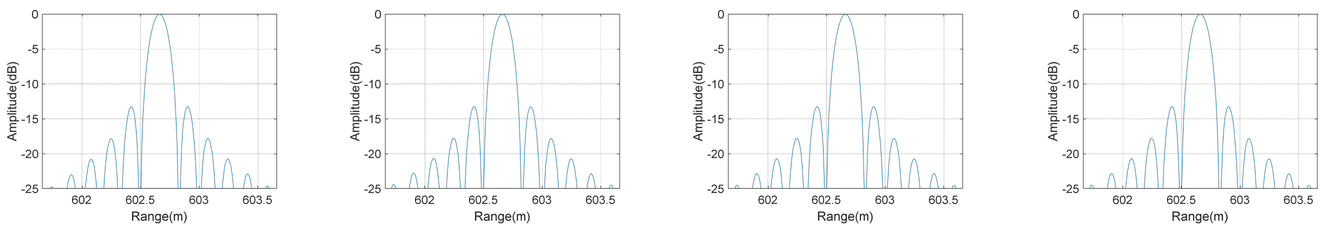

(**a**) (**b**) (**c**) (**d**)

Figure 16. PSF results of point B in range: (**a**) Single-phase-center distribution; (**b**) Sparse multi-phase-center distribution in [25]; (**c**) Optimal sparse multi-phase-center distribution; (**d**) Multi-phase-center distribution with equivalent solid spectrum.

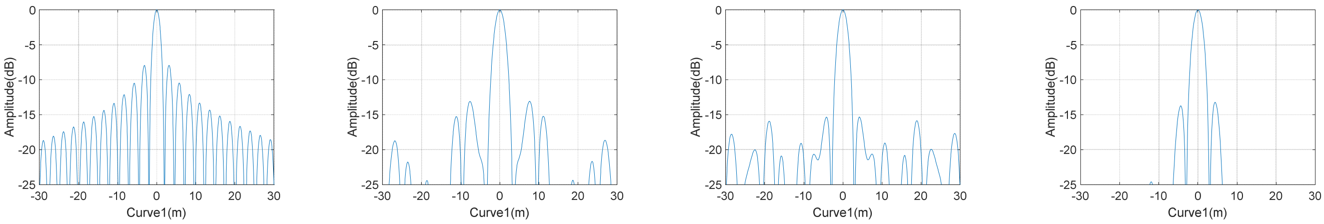

(**a**) (**b**) (**c**) (**d**)

Figure 17. PSF results of point B in Curve1: (**a**) Single-phase-center distribution; (**b**) Sparse multi-phase-center distribution in [25]; (**c**) Optimal sparse multi-phase-center distribution; (**d**) Multi-phase-center distribution with equivalent solid spectrum.

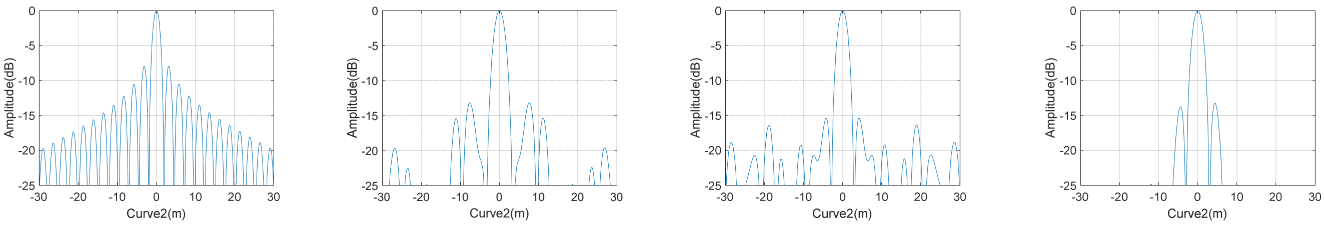

(**a**) (**b**) (**c**) (**d**)

Figure 18. PSF results of point B in Curve2: (**a**) Single-phase-center distribution; (**b**) Sparse multi-phase-center distribution in [25]; (**c**) Optimal sparse multi-phase-center distribution; (**d**) Multi-phase-center distribution with equivalent solid spectrum.

As we can see from Figure 16, the PSF results of point targets at scene edge by circular GBSAR with the four different distributions are also almost identical in range. As shown in Figures 17a and 18a, for point target B, the sidelobes in Curve1 and Curve2 by circular GBSAR with single-phase-center distribution are also high. Figure 17b,c and Figure 18b,c show that the sidelobes of the optimal sparse multi-phase-center circular GBSAR in Curve1 and Curve2 are lower than those of the sparse multi-phase-center distribution in [25]. This shows that the better sidelobe suppression effect of the proposed method is also applicable to point targets at scene edge. It can be seen from Figures 17d and 18d that the PSF results of point B by circular GBSAR based on multi-phase-center distribution with equivalent solid spectrum are almost consistent with those of point A. Table 5 shows the 3D imaging quality parameters of point B by circular GBSAR.

Table 5. The 3D imaging quality analysis of point B.

Array Distribution	Parameters	Range	Curve1	Curve2
Single-phase-center distribution	IRW (m)	0.15	1.85	1.85
	PSLR (dB)	−13.24	−7.93	−7.95
	ISLR (dB)	−10.49	−1.19	−1.38
Sparse multi-phase-center distribution in [25]	IRW (m)	0.15	2.68	2.68
	PSLR (dB)	−13.23	−13.08	−13.16
	ISLR (dB)	−10.45	−5.62	−6.23
Optimal sparse multi-phase-center distribution	IRW (m)	0.15	2.50	2.50
	PSLR (dB)	−13.24	−15.32	−15.35
	ISLR (dB)	−10.46	−6.15	−6.44
Multi-phase-center distribution with equivalent solid spectrum	IRW (m)	0.15	2.65	2.64
	PSLR (dB)	−13.24	−13.22	−13.25
	ISLR (dB)	−10.46	−11.74	−11.79

As shown in Table 5, for point target B, the PSLR and ISLR in Curve1 and Curve2 by circular GBSAR with optimal sparse multi-phase-center distribution are also lower than those of circular GBSAR with single-phase-center distribution and the sparse multi-phase-center distribution in [25]. The PSLR and ISLR of point B by circular GBSAR with four different distributions are very close to those of point A. This indicates that the proposed method also has a better sidelobe suppression effect on point targets at the scene edge.

5. Conclusions

In this paper, we have examined the sidelobe suppression for circular GBSAR 3D imaging. To suppress the high sidelobes of circular GBSAR at low cost, we proposed a sidelobe suppression method for circular GBSAR 3D imaging based on sparse optimization of radial phase-center distribution. By sparsely optimizing the radial phase-center distribution of circular GBSAR, the proposed method can obtain the optimal 3D sidelobe suppression effect of circular GBSAR under the condition of a given number of phase centers. In the example of the number of phase centers $N = 3$, the PSL on the 3D curved surface by circular GBSAR with the optimal sparse phase center distribution obtained by the proposed method has been suppressed to below -13.2 dB, and its ISL has been suppressed to below -6 dB. The results illustrate that the proposed method can effectively suppress the 3D sidelobes of circular GBSAR under the conditions of a limited number of phase centers, further improving the 3D imaging quality of circular GBSAR. In addition, the 3D BP imaging results of the point target show that the 3D imaging quality of circular GBSAR based on optimal sparse phase-center distribution is close to that of circular GBSAR based on phase-center distribution with an equivalent solid spectrum. This shows that the proposed method can obtain 3D SAR images with high quality at low cost and is helpful for measuring accurate deformation of complex terrain areas. Moreover, the applicability of the proposed method to any point targets in the observation scene has been validated by the 3D imaging results of multiple point targets. However, it takes quite a long time to use the BP algorithm for circular GBSAR 3D imaging. The proposed method involves imaging the echo data received from multiple antenna phase centers. Therefore, the proposed method has potentially poor timeliness in practical applications. For further research, we should focus on the 3D fast imaging algorithm for circular GBSAR to improve the timeliness in potential 3D deformation monitoring applications.

Author Contributions: Conceptualization, Q.Z. and Y.W.; methodology, Q.Z. and J.S.; software, Q.Z.; validation, J.S., Y.W. and Y.L.; formal analysis, Y.W.; investigation, Q.Z.; resources, Y.L.; data curation, Q.Z.; writing—original draft preparation, Q.Z.; writing—review and editing, J.S., Y.W. and Y.L.; visualization, Q.Z.; supervision, J.S.; project administration, J.S. and Y.W.; funding acquisition, J.S. All authors have read and agreed to the published version of the manuscript.

Funding: This research was funded by the National Natural Science Foundation of China, Grant Nos. 62131001 and 62171029.

Data Availability Statement: Not applicable.

Conflicts of Interest: The authors declare no conflict of interest.

References

1. Wang, Y.; Hong, W.; Zhang, Y.; Lin, Y.; Li, Y.; Bai, Z.; Zhang, Q.; Lv, S.; Liu, H.; Song, Y. Ground-based Differential Interferometry SAR: A review. *IEEE Geosci. Remote Sens. Mag.* **2020**, *8*, 43–70. [CrossRef]
2. Pieraccini, M.; Miccinesi, L. An Interferometric MIMO Radar for Bridge Monitoring. *IEEE Geosci. Remote Sens. Lett.* **2019**, *16*, 1383–1387. [CrossRef]
3. Dong, L.; Wang, C.; Tang, Y.; Tang, F.; Zhang, H.; Wang, J.; Duan, W. Time Series InSAR Three-Dimensional Displacement Inversion Model of Coal Mining Areas Based on Symmetrical Features of Mining Subsidence. *Remote Sens.* **2021**, *13*, 2143. [CrossRef]
4. Luo, Y.; Song, H.; Wang, R.; Deng, Y.; Zhao, F.; Xu, Z. Arc FMCW SAR and Applications in Ground Monitoring. *IEEE Trans. Geosci. Remote Sens.* **2014**, *52*, 5989–5998. [CrossRef]
5. Zhang, Y.; Wang, Y.; Wei, Y.; Zhao, L.; Bai, W. Spherical Wave Decomposition Based Polar Format Algorithm for ArcSAR Imaging. *IEEE Trans. Geosci. Remote Sens.* **2021**, *59*, 7547–7556. [CrossRef]
6. Zhang, Y.; Wang, Y.; Schmitt, M.; Yuan, C. Efficient ArcSAR Focusing in the Wavenumber Domain. *IEEE Trans. Geosci. Remote Sens.* **2022**, *60*, 1–10. [CrossRef]

7. Wang, S.; Feng, W.; Kikuta, K.; Sato, M. A Monostatic/Bistatic Ground-Based Synthetic Aperture Radar System for Target Imaging and 2-D Displacement Estimation. *IEEE Geosci. Remote Sens. Lett.* **2021**, *18*, 326–330. [CrossRef]
8. Miccinesi, L.; Pieraccini, M. Bridge Monitoring by a Monostatic/Bistatic Interferometric Radar Able to Retrieve the Dynamic 3D Displacement Vector. *IEEE Access* **2020**, *8*, 210339–210346. [CrossRef]
9. Reale, D.; Serafino, F.; Pascazio, V. An Accurate Strategy for 3-D Ground-Based SAR Imaging. *IEEE Geosci. Remote Sens. Lett.* **2009**, *6*, 681–685. [CrossRef]
10. Pieraccini, M.; Rojhani, N.; Miccinesi, L. Ground Based Synthetic Aperture Radar with 3D Imaging Capability. In Proceedings of the 2018 European Radar Conference, Madrid, Spain, 26–28 September 2018; pp. 206–209.
11. Li, Y.; Huo, T.; Yang, C.; Wang, T.; Wang, J.; Li, B. An Efficient Ground Moving Target Imaging Method for Airborne Circular Stripmap SAR. *Remote Sens.* **2022**, *14*, 210. [CrossRef]
12. Yitayew, T.G.; Ferro-Famil, L.; Eltoft, T.; Tebaldini, S. Tomographic Imaging of Fjord Ice Using a Very High Resolution Ground-based SAR System. *IEEE Trans. Geosci. Remote Sens.* **2017**, *55*, 698–714. [CrossRef]
13. Ramachandran, N.; Saatchi, S.; Tebaldini, S.; Mariotti, M.; Dikshit, O. Evaluation of P-Band SAR Tomography for Mapping Tropical Forest Vertical Backscatter and Tree Height. *Remote Sens.* **2021**, *13*, 1485. [CrossRef]
14. Tian, W.; Yang, W.; Dang, T.; Zhao, Z.; Han, X. Three-Dimensional Ground-Based SAR Imaging Algorithm Based on Keystone Formatting and Subblock. *IEEE Access* **2020**, *8*, 90118–90131. [CrossRef]
15. Huang, Z.; Sun, J.; Tan, W.; Huang, P.; Qi, Y. A Fast Far-Field Pseudopolar Format Algorithm for Ground-Based Arc 3-D SAR Imaging. *IEEE Geosci. Remote Sens. Lett.* **2020**, *17*, 1697–1701. [CrossRef]
16. Pieraccini, M.; Agostini, N.; Papi, F.; Rocchio, S. A rotating antenna ground-based SAR. In Proceedings of the 2015 European Radar Conference, Paris, France, 7–10 September 2015; pp. 493–496.
17. Pieraccini, M.; Papi, F.; Rocchio, S. SAR imagery by RotoSAR. In Proceedings of the 2015 IEEE International Conference on Microwaves, Communications, Antennas and Electronic Systems, Tel Aviv, Israel, 2–4 November 2015; pp. 1–5.
18. DeGraaf, S.R. Sidelobe Reduction via Adaptive FIR Filtering in SAR Imagery. *IEEE Trans. Image Process.* **1994**, *3*, 292–301. [CrossRef] [PubMed]
19. Wang, H.; Su, Y.; Xu, H.; Zhu, Y. Sidelobe reduction based on spectrum reshaping in microwave imaging. *Sci. China (Inf. Sci.)* **2011**, *54*, 204–212. [CrossRef]
20. Iglesias, R.; Mallorqui, J. Side-Lobe Cancelation in DInSAR Pixel Selection With SVA. *IEEE Geosci. Remote Sens. Lett.* **2013**, *10*, 667–671. [CrossRef]
21. Ding, Z.; Zhu, K.; Wang, Y.; Li, L.; Liu, M.; Zeng, T. Spatially Variant Sidelobe Suppression for Linear Array MIMO SAR 3-D Imaging. *IEEE Trans. Geosci. Remote Sens.* **2022**, *60*, 11–15. [CrossRef]
22. Li, C.; Yu, Z.; Chen, J. Overview of Techniques for Improving High-resolution Spaceborne SAR Imaging and Image Quality. *J. Radars* **2019**, *8*, 717–731. (In Chinese)
23. Zhu, X.; He, F.; Ye, F.; Dong, Z.; Wu, M. Sidelobe Suppression with Resolution Maintenance for SAR Images via Sparse Representation. *Sensors* **2018**, *18*, 1589. [CrossRef]
24. Ming, J.; Zhang, X.; Pu, L.; Shi, J. PSF Analysis and Ground Test Results of a Novel Circular Array 3-D SAR System. *J. Radars* **2018**, *7*, 770–776. (In Chinese)
25. Wang, Y.; Zhang, Q.; Lin, Y.; Zhao, Z.; Li, Y. Multi-Phase-Center Sidelobe Suppression Method for Circular GBSAR Based on Sparse Spectrum. *IEEE Access* **2020**, *8*, 133802–133816. [CrossRef]
26. Soumekh, M. *Synthetic Aperture Radar Signal Processing with MATLAB Algorithms*; John Wiley & Sons, Inc.: Hoboken, NJ, USA, 1999; pp. 486–552.
27. Deb, K.; Pratap, A.; Agarwal, S.; Meyarivan, T. A Fast and Elitist Multiobjective Genetic Algorithm: NSGA-II. *IEEE Trans. Evolut. Comput.* **2002**, *6*, 182–197. [CrossRef]